

Cite this: *J. Mater. Chem. A*, 2021, 9, 4310

Separated redox site strategies for engineering highly efficient photocatalysts: a pagoda-like $\text{In}_2\text{O}_3/\text{CuO}$ heteroepitaxial structure coated with a N-doped C layer†

Yun Yang, Liming Sun,* Wenwen Zhan, Xiaojun Wang  and Xiguang Han *

In order to prepare efficient photocatalysts, it is necessary to consider not only the generation, separation and migration of photo-generated carriers, but also the effective activation of reactants and the reasonable distribution of redox sites. In this article, we utilized a MOF-on-MOF heterostructure with epitaxial relationship as the precursor to synthesize N-doped C encapsulated pagoda-like $\text{CuO}-\text{In}_2\text{O}_3$ ($\text{In}_2\text{O}_3/\text{CuO}@N-C$) heteroepitaxial micro-rods. In the obtained $\text{In}_2\text{O}_3/\text{CuO}@N-C$ hierarchical pagoda-like micro-rods, the loose lamellar structure enhanced the light-harvesting capability, the formed $\text{CuO}-\text{In}_2\text{O}_3$ p-n heterojunction improved the separation efficiency of photo-generated carriers, and the coated N-doped carbon layer facilitated the transfer of photo-generated carriers and the activation of reactants. More importantly, the directional separation of CuO (external nanosheets) and In_2O_3 (central axis) acted as oxidation and reduction sites to react with 2-phenyl-1,2,3,4-tetrahydroisoquinoline and indole, respectively, which effectively avoided the inverse reaction of cross-dehydrogenative coupling (CDC). Therefore, the obtained pagoda-like $\text{In}_2\text{O}_3/\text{CuO}@N-C$ heteroepitaxial micro-rods exhibited excellent photocatalytic activity for the CDC reaction. The present work provides a new design strategy for the comprehensive construction of a high efficiency photocatalytic material system.

Received 6th November 2020
Accepted 6th January 2021

DOI: 10.1039/d0ta10831f

rsc.li/materials-a

Introduction

With the increasing demand for energy and the increasing shortage of energy, the semiconductor photocatalysis technology, which can convert green and sustainable solar energy into chemical energy, has been widely explored.^{1–5} It is common knowledge that both reductive and oxidative processes involving photo-generated electrons and holes, respectively, occur in a photocatalytic reaction. The effective separation of photo-generated electrons and holes in photocatalysts is the first step to promote a photocatalytic reaction. On the other hand, the interfacial redox reaction, which is usually the direct output of photocatalysis, is considered as the last step of photocatalysis.⁶ Because this interfacial redox reaction contains a series of radical chain reactions, which are often thought to be initiated from the activation of the reactants by photo-generated carriers,^{7–9} and their corresponding

inverse reactions, it is considered to be the most important but complicated process in photocatalysis. Therefore, the efficient separation and migration of photo-generated carriers and the thermodynamic requirements are not enough to achieve a photocatalytic reaction. The effective activation of reactants and the reasonable distribution of redox sites should also be considered,^{10–13} which is very important for the construction of an efficient photocatalyst system.

Recently, the synthesis of carbon-coated semiconductor metal oxide heterostructures by using metal-organic frameworks (MOFs) as precursors has become one of the important means to construct efficient photocatalysts.^{14–29} A photocatalyst prepared by this method has a compact heterojunction interface and a uniformly coated carbon layer, which can ensure the effective separation and smooth migration of photo-generated electrons and holes. In addition, the coated carbon layer can also enhance the adsorption and activation of some reactants,³⁰ especially some organic reactants containing six-membered carbon rings, which is of great significance to expand the application of inorganic photocatalysts in the field of organic reactions. However, the two metal oxide particles in these heterojunction photocatalysts are usually mixed indiscriminately, which makes the redox sites of photocatalysis also randomly distributed. The short distance between the randomly distributed redox sites can lead to the inverse reaction of

Jiangsu Key Laboratory of Green Synthetic Chemistry for Functional Materials, Department of Chemistry, School of Chemistry and Chemical Engineering, Jiangsu Normal University, Xuzhou, 221116, P. R. China. E-mail: xghan@jnsu.edu.cn

† Electronic supplementary information (ESI) available: Experimental details, powder XRD, EDX mapping, FT-IR spectra and TGA curves of MIL-68-In and MIL-68-In@Cu-BDC precursors, the corresponding characterization of reference samples and $\text{In}_2\text{O}_3/\text{CuO}@N-C$ after the catalytic reaction, contrast experiments for the catalyzed CDC reaction and Mulliken charge population. See DOI: 10.1039/d0ta10831f

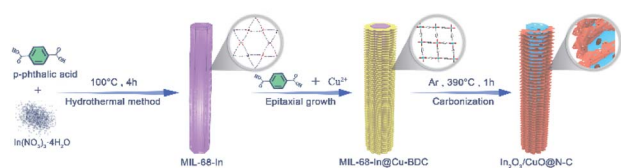
photocatalysis and is not conducive to the interfacial redox reaction.^{31–33}

If utilizing a MOF-on-MOF heterostructure with epitaxial relationship as the precursor, we can not only retain the above advantages in the obtained metal oxide heterojunction, but also directly separate the two kinds of metal oxide particles, so as to realize the effective spatial separation of redox sites in the photocatalysis and inhibit the inverse reaction. Based on this design strategy, in this work, Cu-BDC nano-sheets were epitaxially grown on MIL-68-In micro-rods to form the MIL-68-In@Cu-BDC heterostructure, which was calcined as a precursor to obtain a N-doped C encapsulated CuO–In₂O₃ heteroepitaxial structure (In₂O₃/CuO@N-C) with the morphology of hierarchical pagoda-like micro-rods. The In₂O₃/CuO@N-C hierarchical pagoda-like micro-rods synthesized by this strategy not only have enhanced light absorption capacity, separation efficiency of photo-generated electron–hole pairs and the ability to activate reactants, but also possess directionally separated oxidation (CuO external nanosheets) and reduction (In₂O₃ central axis) sites, which can effectively prevent the occurrence of inverse reactions. The In₂O₃/CuO@N-C hierarchical pagoda-like micro-rods exhibited excellent photocatalytic activity for the CDC reaction under blue LED irradiation as expected. This work would provide a new design idea for the comprehensive construction of a high efficiency photocatalytic material system.

Results and discussion

The synthesis procedure of a N-doped C encapsulated CuO–In₂O₃ heteroepitaxial structure (In₂O₃/CuO@N-C) with the morphology of hierarchical pagoda-like micro-rods is schematically depicted in Scheme 1. A well-defined MIL-68-In precursor with a micro-rod morphology is first synthesized by a solvothermal method in the presence of indium(III) nitrate tetrahydrate (In(NO₃)₃·4H₂O) and 1,4-benzenedicarboxylic acid in *N,N*-dimethylformamide (DMF) at 100 °C for 4 h. After dispersing the obtained MIL-68-In micro-rods in a solution of 1,4-benzenedicarboxylic acid and copper nitrate hexahydrate (Cu(NO₃)₂·6H₂O) at 120 °C for 30 min, Cu-BDC nano-sheets were epitaxially grown on the MIL-68-In micro-rods to form the MIL-68-In@Cu-BDC precursor. The In₂O₃/CuO@N-C can be finally obtained by carbonizing the MIL-68-In@Cu-BDC precursor in an Ar atmosphere at 390 °C for 1 h.

In order to determine the composition and structure of the obtained In₂O₃/CuO@N-C, the MIL-68-In precursor was first characterized. As shown by X-ray powder diffraction (XRD, Fig. S1†), the precursor exhibited sharp diffraction peaks and all



Scheme 1 Schematic illustration showing the synthetic process of monodisperse In₂O₃/CuO@N-C hierarchical pagoda-like micro-rods.

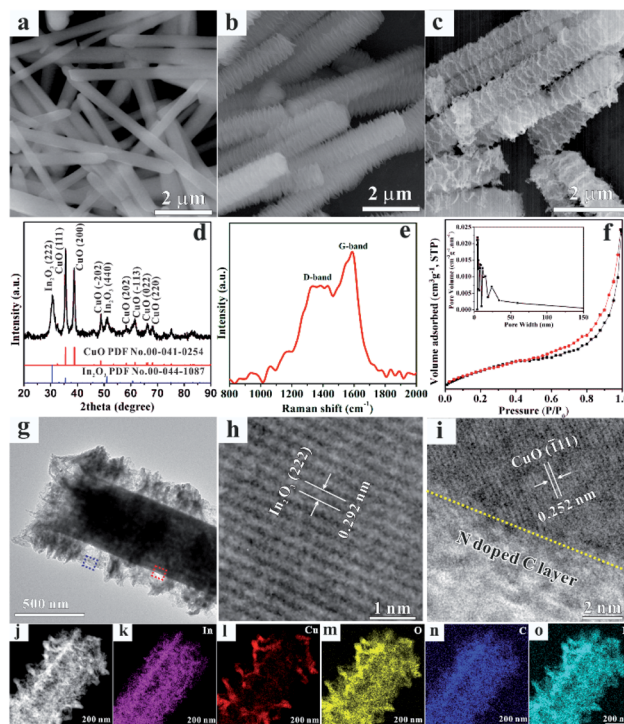


Fig. 1 (a) FE-SEM image of the MIL-68-In precursor; (b) SEM image of the MIL-68-In@Cu-BDC precursor; (c) SEM image, (d) XRD pattern, (e) Raman spectrum, (f) N₂ adsorption/desorption isotherms and BJH pore size distribution of the pagoda-like In₂O₃/CuO@N-C heteroepitaxial structure; (g) TEM image of a typical In₂O₃/CuO@N-C hierarchical pagoda-like micro-rod; (h) HRTEM image of the central axis in the In₂O₃/CuO@N-C hierarchical pagoda-like micro-rods (marked with a red frame in Fig. 1g); (i) HRTEM image of the external sheet in In₂O₃/CuO@N-C hierarchical pagoda-like micro-rods (marked with a blue frame in Fig. 1g); (j) STEM image; and (k)–(o) EDX elemental mapping of In, Cu, O, C and N elements for the In₂O₃/CuO@N-C hierarchical pagoda-like micro-rods.

peaks were consistent with a previous report,³⁴ which confirmed that the obtained precursor was pure phase MIL-68-In with good crystallinity. The image from field emission scanning electron microscopy (FESEM, Fig. 1a) verified the formation of solid MIL-68-In micro-rods with high uniformity and smooth surfaces. Energy-dispersive X-ray spectroscopy (EDX) element mapping (Fig. S2†) indicated that the In, O, C and N elements were evenly dispersed throughout the MIL-68-In rod structure. After adding MIL-68-In precursors in 1,4-benzenedicarboxylic acid and Cu(NO₃)₂·6H₂O solution, the XRD result (Fig. S3†) showed the residual MIL-68-In phase and the presence of the Cu-BDC phase,^{35,36} indicating the formation of the MIL-68-In@Cu-BDC precursor. From the FESEM image (Fig. 1b), it can be found that numerous Cu-BDC nanosheets with an oriented assembly grow epitaxially on the surface of MIL-68-In rods to form the MIL-68-In@Cu-BDC precursor. EDX mapping of the MIL-68-In@Cu-BDC precursor (Fig. S4†) also showed that the In, Cu, O, C and N elements are uniformly distributed in the precursor structure. According to the thermogravimetric analysis (TGA) of the MIL-68-In@Cu-BDC precursor (Fig. S5†), the pyrolysis temperature for the carbonization of the precursor was set to 390 °C.

The typical SEM image (Fig. 1c) of $\text{In}_2\text{O}_3/\text{CuO}@N\text{-C}$ indicated that the hierarchical rod morphology of the MIL-68- $\text{In}@Cu\text{-BDC}$ precursor was well preserved after the annealing process. However, compared with the MIL-68- $\text{In}@Cu\text{-BDC}$ precursor, the distance between the ultrathin nanosheets in $\text{In}_2\text{O}_3/\text{CuO}@N\text{-C}$ hierarchical micro-rods increased, resulting in a pagoda-like structure. Moreover, the ultrathin nanosheet subunit in the $\text{In}_2\text{O}_3/\text{CuO}@N\text{-C}$ hierarchical pagoda-like micro-rods was converted to a porous structure. The XRD pattern (Fig. 1d) indicated that the product after the annealing process was covered with CuO (PDF no. 00-041-0254) and In_2O_3 (PDF no. 00-044-1087) phases. The Raman spectrum of the $\text{In}_2\text{O}_3/\text{CuO}@N\text{-C}$ hierarchical pagoda-like micro-rods (Fig. 1e) presented a D-band at 1385 cm^{-1} (associated with structural disorders and defects) and a G-band at 1588 cm^{-1} (related to graphitic carbon), which indicated the presence of highly disordered/defective graphitic carbon in $\text{In}_2\text{O}_3/\text{CuO}@N\text{-C}$ hierarchical pagoda-like micro-rods. The porous nature of $\text{In}_2\text{O}_3/\text{CuO}@N\text{-C}$ was also examined by N_2 sorption measurement (Fig. 1f), which showed a large Brunauer–Emmett–Teller (BET) surface area of about $147.1\text{ m}^2\text{ g}^{-1}$. According to Barrett–Joyner–Halenda (BJH) analysis (inset of Fig. 1f), the pore size distribution is mainly centered at the mesoporous size range. The hierarchical structure and the inside structural information of $\text{In}_2\text{O}_3/\text{CuO}@N\text{-C}$ hierarchical pagoda-like micro-rods were further characterized by transmission electron microscopy (TEM). From Fig. 1g, it can be seen that the obtained $\text{In}_2\text{O}_3/\text{CuO}@N\text{-C}$ possessed a hierarchical structure with loose and porous characteristics. High resolution transmission electron microscopy (HRTEM) was used to investigate the composition of each part in the $\text{In}_2\text{O}_3/\text{CuO}@N\text{-C}$ hierarchical pagoda-like micro-rods. The HRTEM image of the central axis in $\text{In}_2\text{O}_3/\text{CuO}@N\text{-C}$ hierarchical pagoda-like micro-rods (Fig. 1h) exhibited that the lattice distance was 0.292 nm , which corresponded to the (222) plane of In_2O_3 . On the other hand, a lattice distance of 0.252 nm belonging to the CuO (111) plane appeared in the HRTEM image of the external sheet in $\text{In}_2\text{O}_3/\text{CuO}@N\text{-C}$ hierarchical pagoda-like micro-rods (Fig. 1i). Moreover, from Fig. 1i, it can be found that the CuO was encapsulated by a few layered carbon shell. These results of HRTEM indicated that the central axis of $\text{In}_2\text{O}_3/\text{CuO}@N\text{-C}$ hierarchical pagoda-like micro-rods consisted of In_2O_3 , the external nanosheets were composed of CuO, and the outside of the micro-rods was coated with carbon layers. This conclusion was further verified using the STEM image (Fig. 1j) and energy-dispersive X-ray (EDX) mapping. As shown in Fig. 1k, the In element was concentrated on the central axis of $\text{In}_2\text{O}_3/\text{CuO}@N\text{-C}$ hierarchical pagoda-like micro-rods. On the other hand, the Cu element was distributed on the external nanosheets of $\text{In}_2\text{O}_3/\text{CuO}@N\text{-C}$ hierarchical pagoda-like micro-rods (Fig. 1l). From Fig. 1m–o, it could be found that the O, C and N elements were homogeneously distributed in the hierarchical structure. The EDX mapping results manifested that the $\text{In}_2\text{O}_3/\text{CuO}@N\text{-C}$ hierarchical pagoda-like micro-rods were composed of the In_2O_3 central axis and CuO external sheets, and coated by N-doped C layers, and they were consistent with the results of HRTEM.

Moreover, X-ray photoelectron spectroscopy (XPS) was used to investigate the surface elemental chemical compositions and the chemical state of $\text{In}_2\text{O}_3/\text{CuO}@N\text{-C}$ hierarchical micro-rods. The survey spectrum indicated the existence of In, Cu, O, C, and N elements in the $\text{In}_2\text{O}_3/\text{CuO}@N\text{-C}$ hierarchical micro-rods (Fig. 2a). The high resolution XPS spectrum of Cu 2p was recorded and is shown in Fig. 2b. The two main peaks at 953.8 and 933.4 eV corresponded to Cu 2p_{1/2} and Cu 2p_{3/2}, and the distance between the two peaks was 20 eV, implying a normal state of Cu^{2+} . Moreover, the shake-up satellites (denoted as Sat.) at 941.4, 943.9 and 962.6 eV, which are unique characteristics of Cu^{2+} , also confirm the presence of CuO. Fig. 2c shows the In 3d XPS spectrum with double peaks, which were attributed to typical spin–orbit split In 2d_{5/2} (444.7 eV) and In 2d_{3/2} (452.3 eV), respectively. The result indicated that In(III) was the predominant state in the sample. The high-resolution O 1s spectrum (Fig. 2d) could be deconvoluted into three major peaks centered at 529.9, 530.7 and 531.9 eV corresponding to the lattice oxygen (O_V), C=O, and O–H bonds, respectively. The C 1s spectrum (Fig. 2e) was composed of four deconvoluted peaks. The peaks at 284.7 eV corresponded to the C=C/C–C bonds. The peak at 285.6 eV was assigned to the C–N bond, which confirmed the nitrogen-doping in the carbon layer. The carbon atoms bonded to the carbonyl group (C–O) were represented by the peak at 288.9 eV. The peaks of N 1s (Fig. 2f) can be ascribed to graphene-N (400.1 eV). Therefore, by combining XPS, HRTEM and EDX mapping analyses of $\text{In}_2\text{O}_3/\text{CuO}@N\text{-C}$, it can be concluded that

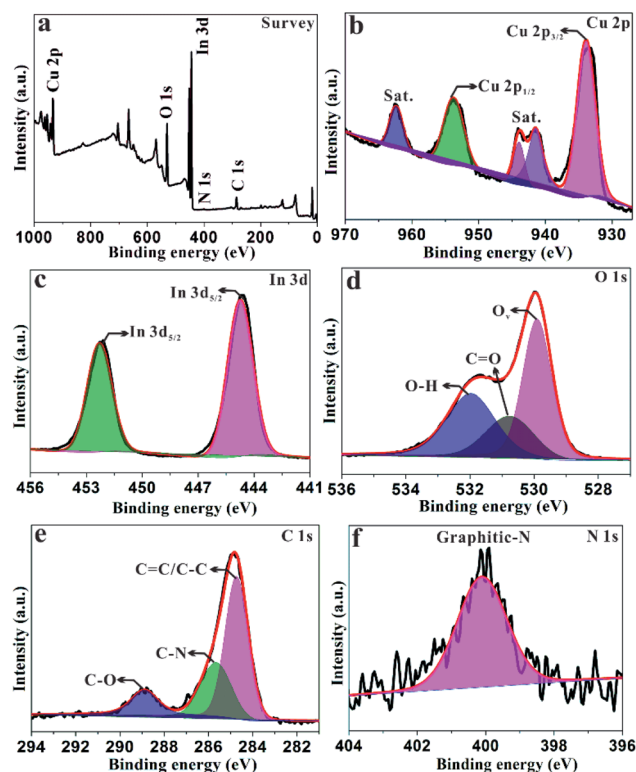


Fig. 2 XPS spectrum of $\text{In}_2\text{O}_3/\text{CuO}@N\text{-C}$ hierarchical pagoda-like micro-rods, (a) survey spectrum and high-resolution XPS spectrum: (b) Cu 2p, (c) In 3d, (d) O 1s, (e) C 1s, and (f) N 1s.

N-doped C layer-coated hierarchical pagoda-like micro-rods, which were constituted by the In_2O_3 central axis and CuO external nanosheets, have been fabricated.

The formation of $\text{In}_2\text{O}_3/\text{CuO}$ heterojunctions and an external N-doped C layer offered directional transfer channels for photo-generated electrons, which could effectively increase the separation efficiency of electrons and holes. In order to characterize the migration and separation of photo-generated electrons and holes, linear sweep voltammetry (LSV) curves, photocurrent density potential (PDP), electrochemical impedance spectra (EIS) and photoluminescence spectra of four samples ($\text{In}_2\text{O}_3/\text{CuO}@N\text{-C}$, $\text{In}_2\text{O}_3@N\text{-C}$ (corresponding preparation and characterization are shown in ESI Fig. S6†), $\text{CuO}@N\text{-C}$ (Fig. S7†) and $\text{In}_2\text{O}_3/\text{CuO}$ (Fig. S8†)) have been characterized, respectively. The LSV curves (Fig. 3a) showed that the $\text{In}_2\text{O}_3/\text{CuO}@N\text{-C}$ has a higher cathodic current density for the reduction of water to H_2 than $\text{In}_2\text{O}_3@N\text{-C}$, $\text{CuO}@N\text{-C}$ and $\text{In}_2\text{O}_3/\text{CuO}$, resulting from the accelerated charge transfer ability caused by the synergistic effects of the $\text{In}_2\text{O}_3/\text{CuO}$ heterojunctions and N-doped C layer coating. The separation efficiency of photo-generated electrons and holes was directly characterized by measuring the photocurrent density of four different samples. As shown in Fig. 3b, $\text{In}_2\text{O}_3/\text{CuO}@N\text{-C}$ exhibited higher photo-current density than $\text{In}_2\text{O}_3@N\text{-C}$ and $\text{CuO}@N\text{-C}$ samples, respectively, indicating that the presence of $\text{In}_2\text{O}_3/\text{CuO}$ heterojunctions can increase the separation efficiency. Furthermore, $\text{In}_2\text{O}_3/\text{CuO}@N\text{-C}$ showed higher photo-current density than $\text{In}_2\text{O}_3/\text{CuO}$, which proved that the N-doped C layer can further accelerate the electron transfer, promoting the separation of photo-generated electrons and holes in space. The EIS results (Fig. 3c) indicated that the $\text{In}_2\text{O}_3/\text{CuO}@N\text{-C}$ sample has the smallest semicircle in the Nyquist plot among these four samples. The smallest semicircle indicated the lowest charge-transfer resistance, which could warrant efficient transportation and separation of photo-generated carriers. Based on the above results and discussion,

the $\text{In}_2\text{O}_3/\text{CuO}@N\text{-C}$ sample possessed improved separation efficiency of photo-generated electron-hole pairs due to $\text{In}_2\text{O}_3/\text{CuO}$ heterojunctions and the external N-doped C layer. Photoluminescence (PL) emission spectra of the photocatalysts also provided information on charge-separation efficiency. As shown in Fig. 3d, the PL intensity presented a clear trend of $\text{In}_2\text{O}_3/\text{CuO}@N\text{-C} < \text{In}_2\text{O}_3@N\text{-C} < \text{CuO}@N\text{-C} < \text{In}_2\text{O}_3/\text{CuO}$, which indicated that $\text{In}_2\text{O}_3/\text{CuO}@N\text{-C}$ possessed the highest separation rate of photo-induced charges among these samples. A uniform coating of the N-doped carbon layer and heterojunctions were the determining factors responsible for this order of charge separation efficiency. Thus, the obtained $\text{In}_2\text{O}_3/\text{CuO}@N\text{-C}$ hierarchical pagoda-like micro-rods possessed good separation efficiency of photo-generated electron-hole pairs.

The cross-dehydrogenative coupling (CDC) reaction was used as the target reaction to investigate the visible-light photocatalytic activity of $\text{In}_2\text{O}_3/\text{CuO}@N\text{-C}$ hierarchical pagoda-like micro-rods. In order to determine the conditions for photocatalysis, comparative experiments have been performed in the absence of light and a catalyst (Table S1†). The result indicated that this reaction did not occur without any one of them (light and catalyst). Therefore, the photocatalytic reaction was carried out under blue light emitting diode (LED, $\lambda = 450$ nm, 3 W) irradiation in a Schlenk tube (Fig. 4a). In order to systematically study the influence of composition and structure on the photocatalytic activity of $\text{In}_2\text{O}_3/\text{CuO}@N\text{-C}$ hierarchical pagoda-like micro-rods, $\text{In}_2\text{O}_3@N\text{-C}$, $\text{CuO}@N\text{-C}$, $\text{In}_2\text{O}_3/\text{CuO}$ and DNCPH (dodecahedral N-doped C-coated $\text{In}_2\text{O}_3/\text{CuO}$ p-n heterojunction, the corresponding preparation and characterization are shown in ESI Fig. S9†) were used as reference samples. The composition of reference sample DNCPH was the same as that of the $\text{In}_2\text{O}_3/\text{CuO}@N\text{-C}$ hierarchical pagoda-like micro-rods, that is, it was also composed of N-doped C-coated $\text{In}_2\text{O}_3/\text{CuO}$ nanoparticles. However, different from the directional separation arrangement of In_2O_3 and CuO in $\text{In}_2\text{O}_3/\text{CuO}@N\text{-C}$ hierarchical pagoda-like micro-rods, In_2O_3 and CuO nanoparticles were irregularly mixed in DNCPH. As shown in Fig. 4b, the photocatalytic activities of $\text{In}_2\text{O}_3/\text{CuO}@N\text{-C}$ hierarchical pagoda-like micro-rods and DNCPH were higher than those of $\text{In}_2\text{O}_3@N\text{-C}$, $\text{CuO}@N\text{-C}$ and $\text{In}_2\text{O}_3/\text{CuO}$. The ^1H NMR spectra of the reactants and product are shown in Fig. S10.† The results indicated that the $\text{In}_2\text{O}_3/\text{CuO}$ heterostructure and N-doped C layer played a positive effect on the photocatalytic CDC reaction. Compared with DNCPH, the better photocatalytic activity of $\text{In}_2\text{O}_3/\text{CuO}@N\text{-C}$ hierarchical pagoda-like micro-rods declared that the heterojunction structure of the In_2O_3 and CuO directional separation arrangement was more conducive to the CDC reaction. The reason for this phenomenon was that in $\text{In}_2\text{O}_3/\text{CuO}@N\text{-C}$ hierarchical pagoda-like micro-rods, In_2O_3 and CuO separated in space were used as reduction and oxidation sites to enrich photo-generated electrons and photo-generated holes, respectively, which not only realized the effective separation of photo-generated electron-hole pairs, but also effectively inhibited the inverse reaction of the photocatalytic CDC reaction. The cycling stability of the $\text{In}_2\text{O}_3/\text{CuO}@N\text{-C}$ catalysts was checked by repeating the same reaction process for four cycles. As shown in Fig. 4c, $\text{In}_2\text{O}_3/\text{CuO}@N\text{-C}$ catalysts exhibited high

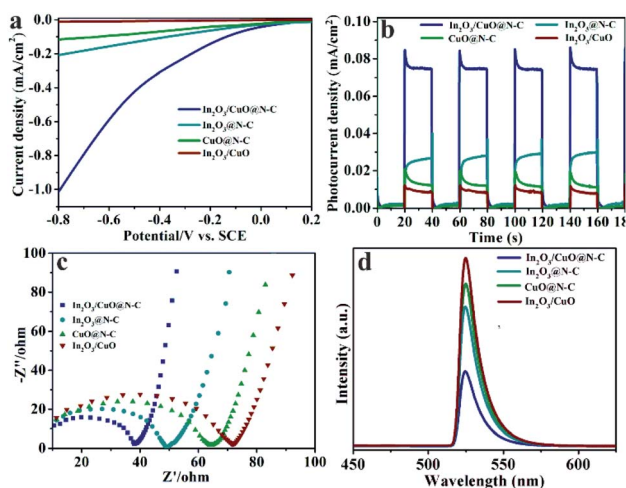


Fig. 3 (a) Linear sweep voltammetry (LSV) curves, (b) photo-current density curves, (c) electrochemical impedance spectroscopy Nyquist plots, (d) photoluminescence spectra of $\text{In}_2\text{O}_3/\text{CuO}@N\text{-C}$, $\text{In}_2\text{O}_3@N\text{-C}$, $\text{CuO}@N\text{-C}$ and $\text{In}_2\text{O}_3/\text{CuO}$ samples.

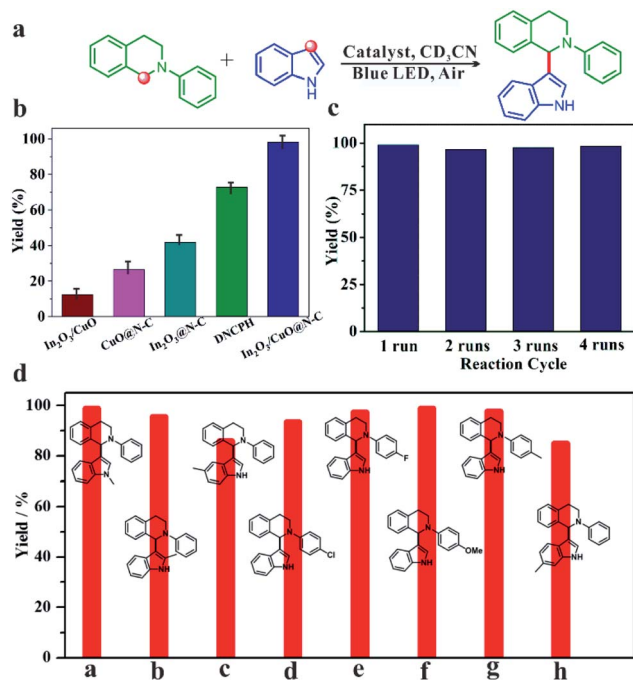


Fig. 4 (a) Photocatalytic equation and conditions of the CDC reaction, (b) reactant yield with In₂O₃/CuO@N-C, In₂O₃@N-C, CuO@N-C, DNCPH and In₂O₃/CuO as photocatalysts, (c) cycling stability using In₂O₃/CuO@N-C as the photocatalyst, and (d) photocatalytic performance of In₂O₃/CuO@N-C in various indole substrates with different *N*-aryl-tetrahydroisoquinoline derivatives.

performance cycling stability without any obvious loss of photocatalytic efficiency. The catalysts well maintained their crystal structure and morphology after four cycles of photocatalytic reaction (Fig. S11[†]). Various indole substrates were reacted with different *N*-aryl-tetrahydroisoquinoline derivatives, and the yields of coupling target products were about 88–99% in each case (Fig. 4d). The above results showed that the In₂O₃/CuO@N-C catalysts exhibited excellent catalytic efficiency and high stability for the CDC photocatalytic reaction.

The activation effect of the carbon layer on reactants was investigated using the electron density difference maps of 2-phenyl-1,2,3,4-tetrahydroisoquinoline and indole before and after adsorption on the graphite (001) surface. The calculated adsorption energies for 2-phenyl-1,2,3,4-tetrahydroisoquinoline and indole on the graphite (001) surface were -0.67 and -0.45 eV, respectively. The corresponding geometric configurations of 2-phenyl-1,2,3,4-tetrahydroisoquinoline and indole adsorbed on the graphite (001) surface are shown in Fig. S12.[†] By comparing the electron density difference maps of 2-phenyl-1,2,3,4-tetrahydroisoquinoline before (Fig. 5a) and after (Fig. 5b) adsorption on the graphite (001) surface, it can be found that the charge redistribution occurred between C_a and H atoms. Compared with that before adsorption, the charge exchange between C_a and H₁ atoms of 2-phenyl-1,2,3,4-tetrahydroisoquinoline after adsorption became weaker. The calculated Mulliken charge on C_a increased from $-0.46e$ to $-0.42e$, meanwhile, the Mulliken charge on H₁ decreased from

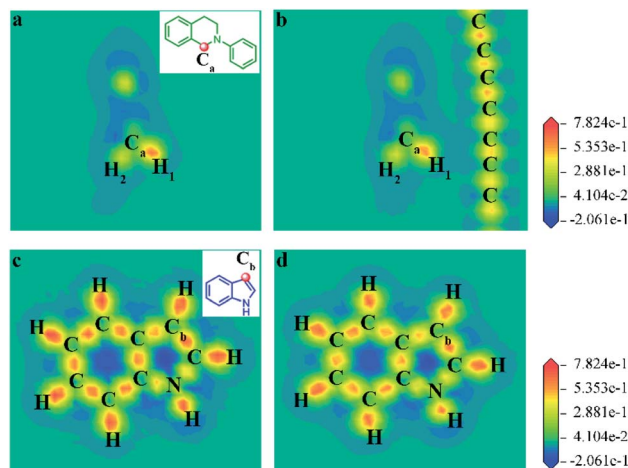
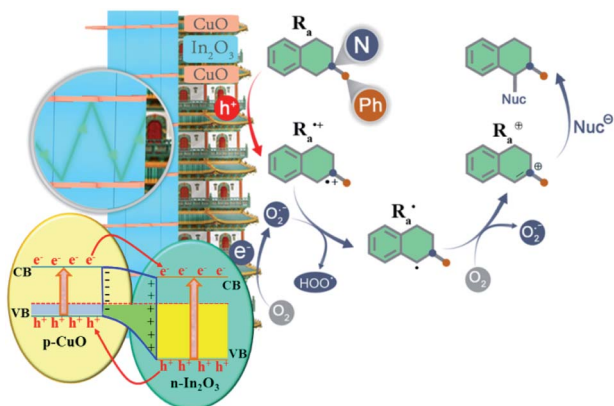


Fig. 5 Electron density difference maps of 2-phenyl-1,2,3,4-tetrahydroisoquinoline (a) before and (b) after the adsorption on the graphite (001) surface; electron density difference maps of indole (c) before and (d) after the adsorption on the graphite (001) surface.

0.31e to 0.27e (Table S2[†]). The bond length of C_a–H₁ stretched from 1.11 Å to 1.12 Å. The charge redistribution and the elongated bond length indicated that the interaction between C_a and H₁ was weakened and the C_a site was activated. As a result, the activated C_a site was easily attacked by the active group and then dehydrogenated. Similar activation also occurred when indole was adsorbed on the graphite (001) surface. After adsorption (Fig. 5d), the charge exchange between the C_b atom and its bonding H atom decreased compared with that before adsorption (Fig. 5c). The Mulliken charge on C_b and its bonding H increased from $-0.40e$ to $-0.39e$ and decreased from $0.33e$ to $0.32e$, respectively. The bond length of C_a–H was elongated from 1.08 Å to 1.09 Å. In the adsorbed indole molecule, the C_b site was activated and can be attacked leading to dehydrogenation. The results of the above theoretical calculation indicated that the coated carbon layer in the In₂O₃/CuO@N-C hierarchical pagoda-like micro-rods has a good adsorption and activation effect on the two reactants (2-phenyl-1,2,3,4-tetrahydroisoquinoline and indole) of the CDC reaction.

Based on the above experimental and theoretical analyses, the possible mechanism of the CDC photocatalytic reaction catalysed by In₂O₃/CuO@N-C hierarchical pagoda-like micro-rods is proposed and shown in Scheme 2. The loose lamellar structure of In₂O₃/CuO@N-C hierarchical pagoda-like micro-rods provided a structural basis for the multi-level reflection of incident light between CuO nanosheets, which was conducive to improving the utilization of incident light and generated more photo-generated electron–hole pairs. The UV-vis absorption spectra of In₂O₃/CuO@N-C, In₂O₃@N-C, CuO@N-C and In₂O₃/CuO were investigated (Fig. S13[†]) and they verified this conclusion. Under blue LED light irradiation, electrons were excited from the valence band (VB) of CuO to its conduction band (CB), leaving holes in the VB. The photo-generated electrons then transferred to the CB of In₂O₃, due to the formation of CuO–In₂O₃ p–n heterojunctions.¹⁶ In order to further investigate the migration path of photo-generated electrons in the



Scheme 2 Schematic showing the proposed mechanism of the CDC photocatalytic reaction catalysed by $\text{In}_2\text{O}_3/\text{CuO}@N\text{-C}$ hierarchical pagoda-like micro-rods.

$\text{In}_2\text{O}_3/\text{CuO}@N\text{-C}$ composites, the highest occupied molecular orbital (HOMO) and the lowest unoccupied molecular orbital (LUMO) of the In_2O_3 (100)/N-doped graphite (001) interface were calculated at the Γ -point (Fig. S14[†]). It could be found that the electronic densities of the HOMO are almost localized around the O atoms of In_2O_3 , while the electronic densities of the LUMO are attributed to the N and C atoms of graphite. This indicated that the photo-generated electrons accumulated on In_2O_3 would further migrate to the coated N-doped carbon layer. So far, the photo-generated electrons and holes were separated in space. The photo-generated holes on CuO nanosheets reacted with 2-phenyl-1,2,3,4-tetrahydroisoquinoline (R_a) to form the radical cation $R_a^{+\bullet}$ as a result of the existence of lone-pair electrons on the N atom in R_a . However, the photo-generated electrons on the In_2O_3 central axis reduced oxygen molecules to superoxide radicals ($\text{O}_2^{\bullet-}$). The generation of $\text{O}_2^{\bullet-}$ in the $\text{In}_2\text{O}_3/\text{CuO}@N\text{-C}$ photocatalyst was further proved by using the N,N,N',N' -tetramethyl-phenylenediamine (TMPD) reagent. The principle of detection was based on the fact that photogenerated electrons can transfer from the TMPD molecule to O_2 , which can produce $\text{O}_2^{\bullet-}$ and a blue-colored product (absorption peaks at 612 nm and 563 nm); therefore, the amount of free radicals could be determined by detecting the intensity of the two absorption peaks. Five samples ($\text{In}_2\text{O}_3/\text{CuO}@N\text{-C}$, DNCPH, $\text{In}_2\text{O}_3@N\text{-C}$, $\text{CuO}@N\text{-C}$ and $\text{In}_2\text{O}_3/\text{CuO}$) produced characteristic absorption peaks after reacting with TMPD (Fig. S15[†]). The characteristic absorption peak intensity of these five samples followed the order of $\text{In}_2\text{O}_3/\text{CuO}@N\text{-C} > \text{DNCPH} > \text{In}_2\text{O}_3@N\text{-C} > \text{CuO}@N\text{-C} > \text{In}_2\text{O}_3/\text{CuO}$, which corresponded well with the trend of the separation and migration ability of photogenerated carriers. The generated $\text{O}_2^{\bullet-}$ attacked the C_a site of R_a activated by the coated carbon layer and captured the H atom on this site to form the intermediate R_a^{\bullet} . Furthermore, the intermediate R_a^{\bullet} was oxidized to the imine cation R_a^{\oplus} . The activated C_b site of indole due to adsorption on the coated carbon layer accepted the photo-generated electrons on In_2O_3 and dehydrogenated to produce the nucleophile (Nuc^-), which attacked the R_a^{\oplus} to afford the final product. In

order to verify the active group of this CDC photocatalytic reaction catalyzed by $\text{In}_2\text{O}_3/\text{CuO}@N\text{-C}$ composites, 2,2,6,6-tetramethylpiperidine-1-oxyl (TEMPO), a well-known $\text{O}_2^{\bullet-}$ scavenger, was added to the reaction mixture under standard conditions. Compared with the 99% yield of the product in the absence of TEMPO, only 7.4% yield of the product was obtained in its presence. Combined with the experimental results that the $\text{In}_2\text{O}_3/\text{CuO}@N\text{-C}$ composites generated a large number of $\text{O}_2^{\bullet-}$ radicals, it could be inferred that the $\text{O}_2^{\bullet-}$ radicals were the main active groups in this CDC photocatalytic reaction.

Conclusions

In summary, the novel $\text{In}_2\text{O}_3/\text{CuO}@N\text{-C}$ hierarchical pagoda-like micro-rods with effective separation of redox sites have been successfully synthesized by utilizing a MOF-on-MOF heterostructure with epitaxial relationship as the precursor. The obtained $\text{In}_2\text{O}_3/\text{CuO}@N\text{-C}$ possessed good separation efficiency of photo-generated electron-hole pairs, attributed to the formation of the CuO- In_2O_3 p-n heterojunction. The loose lamellar structure of $\text{In}_2\text{O}_3/\text{CuO}@N\text{-C}$ hierarchical pagoda-like micro-rods enhanced the light-harvesting capability by the multi-level reflection of incident light between CuO nanosheets. For the CDC photocatalytic reaction, the coated N-doped carbon layer not only ensured the effective separation and smooth migration of photo-generated electrons and holes, but also had a significant activation effect on both reactants (2-phenyl-1,2,3,4-tetrahydroisoquinoline and indole). The directional separation of CuO (external nanosheets) and In_2O_3 (central axis) as oxidation and reduction sites was important to react with 2-phenyl-1,2,3,4-tetrahydroisoquinoline and indole, respectively, which effectively avoids the inverse reaction of CDC. Therefore, the obtained $\text{In}_2\text{O}_3/\text{CuO}@N\text{-C}$ hierarchical pagoda-like micro-rods exhibited excellent photocatalytic activity for the CDC reaction.

Conflicts of interest

There are no conflicts to declare.

Acknowledgements

This work was supported by the National Natural Science Foundation of China (21671085, 21701063 and 22005126), the Natural Science Foundation of Jiangsu Province (BK20191466) and Xuzhou City (KC20061), the Project Funded by the Priority Academic Program Development of Jiangsu Higher Education Institutions, the Postgraduate Research and Practical Innovation Program of Jiangsu Province (KYCX20_2251), and the Jiangsu Overseas Visiting Scholar Program for University Prominent Yong & Middle-Aged Teachers and Presidents.

References

- Z. Zou, J. Ye, K. Sayama and H. Arakawa, *Nature*, 2001, **414**, 625–627.

- 2 K. Maeda and K. Domen, *J. Phys. Chem. Lett.*, 2010, **1**, 2655–2661.
- 3 F. E. Osterloh, *Chem. Soc. Rev.*, 2013, **42**, 2294–2320.
- 4 W. Tu, Y. Zhou and Z. Zou, *Adv. Funct. Mater.*, 2013, **23**, 4996–5008.
- 5 A. Kubacka, M. Fernández-García and G. Colón, *Chem. Rev.*, 2012, **112**, 1555–1614.
- 6 C. Chen, T. Shi, W. Chang and J. Zhao, *ChemCatChem*, 2015, **7**, 724–731.
- 7 A. J. Nozik and R. Memming, *J. Phys. Chem.*, 1996, **100**, 13061–13078.
- 8 A. Hagfeldt and M. Graetzel, *Chem. Rev.*, 1995, **95**, 49–68.
- 9 C. Chen, W. Ma and J. Zhao, *Chem. Soc. Rev.*, 2010, **39**, 4206–4219.
- 10 A. Li, T. Wang, X. X. Chang, W. T. Cai, P. Zhang, J. J. Zhang and J. L. Gong, *Chem. Sci.*, 2016, **7**, 890–895.
- 11 A. Li, T. Wang, X. X. Chang, Z.-J. Zhao, C. C. Li, Z. Q. Huang, P. P. Yang, G. Y. Zhou and J. L. Gong, *Chem. Sci.*, 2018, **9**, 5334–5340.
- 12 P. F. Tan, A. Q. Zhu, L. L. Qiao, W. X. Zeng, H. Cui and J. Pan, *J. Colloid Interface Sci.*, 2019, **533**, 452–462.
- 13 A. Li, X. X. Chang, Z. Q. Huang, C. C. Li, Y. J. Wei, L. Zhang, T. Wang and J. L. Gong, *Angew. Chem., Int. Ed.*, 2016, **55**, 13734–13738.
- 14 C. Y. Jin, M. Wang, Z. L. Li, J. Kang, Y. Zhao, J. Han and Z. M. Wu, *Chem. Eng. J.*, 2020, **398**, 125569.
- 15 C. C. Hu, X. X. Hu, R. Li and Y. J. Xing, *J. Hazard. Mater.*, 2020, **385**, 121599.
- 16 L. M. Sun, Y. Zhuang, Y. S. Yuan, W. W. Zhan, X. J. Wang, X. G. Han and Y. L. Zhao, *Adv. Energy Mater.*, 2019, **9**, 1902839.
- 17 Y. Zhuang, L. M. Sun, S. Y. Zeng, W. W. Zhan, X. J. Wang, Y. L. Zhao and X. G. Han, *Chem.–Eur. J.*, 2019, **25**, 14233–14239.
- 18 T. Guo, K. Wang, G. K. Zhang and X. Y. Wu, *Appl. Surf. Sci.*, 2019, **469**, 331–339.
- 19 J. T. Ren, K. Yuan, K. Wu, L. Zhou and Y. W. Zhang, *Inorg. Chem. Front.*, 2019, **6**, 366–375.
- 20 L. Lin, S. Y. Huang, Y. X. Zhu, B. Du, Z. H. Zhang, C. Chen, X. W. Wang and N. Zhang, *Dalton Trans.*, 2019, **48**, 2715–2721.
- 21 L. L. Lu, B. Y. Wu, W. Shi and P. Cheng, *Inorg. Chem. Front.*, 2019, **6**, 3456–3467.
- 22 X. B. Hou, S. L. Stanley, M. Zhao, J. Zhang, H. M. Zhou, Y. B. Cai, F. L. Huang and Q. F. Wei, *J. Alloys Compd.*, 2019, **777**, 982–990.
- 23 X. X. Zhao, J. R. Feng, J. W. Liu, J. Lu, W. Shi, G. M. Yang, G. C. Wang, P. Y. Feng and P. Cheng, *Adv. Sci.*, 2018, **5**, 1700590.
- 24 S. N. Xiao, D. L. Pan, R. Liang, W. R. Dai, Q. T. Zhang, G. Q. Zhang, C. L. Su, H. X. Li and W. Chen, *Appl. Catal., B*, 2018, **236**, 304–313.
- 25 S. Q. Chen, J. G. Yu and J. Zhang, *J. CO₂ Util.*, 2018, **24**, 548–554.
- 26 Y. Zhang, J. B. Zhou, W. Q. Cai, J. Zhou and Z. Li, *Appl. Surf. Sci.*, 2018, **430**, 549–560.
- 27 Q. Qi, S. J. Liu, X. Li, C. L. Kong, Z. Y. Guo and L. Chen, *J. Solid State Chem.*, 2017, **255**, 108–114.
- 28 Y. Xu, S. M. Wu, X. L. Li, Y. H. Huang, Z. P. Wang, Y. D. Han, J. B. Wu, H. Meng and X. Zhang, *New J. Chem.*, 2017, 15422–15438.
- 29 H. Wang, X. Z. Yuan, Y. Wu, G. M. Zeng, X. H. Chen, L. J. Leng and H. Li, *Appl. Catal., B*, 2015, **174–175**, 445–454.
- 30 L. M. Sun, Y. S. Yuan, R. Li, W. W. Zhan, X. J. Wang, Y. L. Zhao and X. G. Han, *J. Mater. Chem. A*, 2019, **7**, 25423–25432.
- 31 A. Li, T. Wang, X. Chang, W. Cai, P. Zhang, J. Zhang and J. Gong, *Chem. Sci.*, 2016, **7**, 890–895.
- 32 L. Mu, Y. Zhao, A. Li, S. Wang, Z. Wang, J. Yang, Y. Wang, T. Liu, R. Chen, J. Zhu, F. Fan, R. Li and C. Li, *Energy Environ. Sci.*, 2016, **9**, 2463–2469.
- 33 S. Wang, Y. Guan, L. Lu, Z. Shi, S. Yan and Z. Zou, *Appl. Catal., B*, 2018, **224**, 10–16.
- 34 R. Li, L. M. Sun, W. W. Zhan, Y. A. Li, X. J. Wang and X. G. Han, *J. Mater. Chem. A*, 2018, **6**, 15747–15754.
- 35 H. Li, M. Eddaoudi, T. L. Groy and O. M. Yaghi, *J. Am. Chem. Soc.*, 1998, **120**, 8571–8572.
- 36 Z. X. Li, J. M. Chu, D. Meng, Y. Y. Wen, X. F. Xing, H. Miao, M. L. Hu, C. C. Yu, Z. T. Wei, Y. Yang and Y. L. Li, *ACS Catal.*, 2019, **9**, 8659–8668.